Chemical Science

Accepted Manuscript

This article can be cited before page numbers have been issued, to do this please use: Q. Zhou, L. Bao, R. Liu, Z. Sun, Z. Ye, L. Jiao, W. Fan, Y. Zou, H. Yang and J. Wu, *Chem. Sci.*, 2026, DOI: 10.1039/D6SC00676K.

ROYAL SOCIETY OF CHEMISTRY

rsc.li/chemical-science

View Article Online
DOI: 10.1039/D6SC00676K

ARTICLE

π-Aggregation-Free, Fused Perylene Pentamers: Synthesis, Narrowband Far-Red to Near-Infrared Emission, and Chiroptical Properties

Received 00th January 20xx,
Accepted 00th January 20xx

DOI: 10.1039/x0xx00000x

Qifeng Zhou,[a#] Lin-Tao Bao,[b#] Rui Liu,[a#] Zhitao Sun,[a] Zhuolin Ye,[a] Liuying Jiao,[a] Wei Fan,[ac] Ya Zou,*[a] Hai-Bo Yang*[b] and Jishan Wu*[a]

Chiral nanographenes have emerged as promising materials for chiral optoelectronics owing to their intrinsic chiroptical properties. However, their development remains constrained by synthetic challenges, strong π–aggregation, and low fluorescence quantum yields, while emission extending to the near-infrared (NIR) region is still rare. Here, we present a molecular design strategy that combines structural multiplicity with π-extension in a butterfly-shaped fused perylene pentamer scaffold to achieve active circularly polarized luminescence (CPL) emitters. By tuning the Scholl reaction conditions, we selectively obtained either racemic **1a** (**1a-*rac***) together with its *meso*-isomer (**1a-*meso***) or an extended series of nanographenes (**1a**–**1d**). X-ray crystallography revealed contorted architectures featuring helicene subunits, while bulky aryl substituents improved solubility, enhanced stability, and enabled enantiomer separation. Owing to their extended π-conjugation, perylene-like frontier orbital distribution, and increased molecular symmetry and rigidity, these nanographenes exhibit highly tunable and remarkable optical and chiroptical properties. Notably, **1a** demonstrates outstanding chiroptical performance (Φ_F = 65%, B_{CPL} = 66.7 M^{-1} cm^{-1}), whereas **1d** exhibits narrowband emission (FWHM = 37 nm) spanning the far-red to near-infrared region.

Introduction

Chiral nanographenes are an unconventional class of π-conjugated materials that deviate from planar graphene fragments and have attracted increasing interest due to their unique electronic structures, pronounced molecular chirality, and intriguing optical properties.[1] Unlike planar graphene cutouts, chiral nanographenes incorporate helicenes or contorted polycyclic aromatic hydrocarbons, resulting in three-dimensional architectures.[2] The combination of extended π-electron delocalization and structural chirality gives rise to strong electronic circular dichroism (ECD) and circularly polarized luminescence (CPL),[3] enabling applications in circularly polarized organic light-emitting diodes (CP-OLEDs),[4] spin filters,[5] and chiral photodetectors.[6] This integration of π-extension and chirality has thus emerged as a powerful design paradigm for functional organic materials, with numerous studies reporting diverse chiral nanographenes featuring novel topologies and pronounced chiroptical responses.[7]

Despite these advances, achieving chiral nanographenes that combine high fluorescence quantum yields (Φ_F), strong CPL, and emission extending into the near-infrared (NIR) region (>800 nm) remains challenging.[8] Extended π-systems are prone to strong intermolecular π–π interactions, which induce aggregation-caused quenching (ACQ) and reduce luminescence efficiency.[9] For CPL-active materials, suppressed emission directly limits CPL brightness (B_{CPL}),[10] defined as the product of Φ_F and the luminescence dissymmetry factor (g_{lum}).[11] Designing nanographenes that resist π-aggregation while maintaining rigidity and extended conjugation therefore remains a key bottleneck.[12] Furthermore, while most studies focus on visible-light chiral emitters,[13] efficient far-red to NIR chiral emitter is rare yet highly desirable for bioimaging,[14] biosensing,[15] and optoelectronic applications.[16] Achieving far-red to NIR emission is challenging because the energy gap law predicts lower quantum yields at longer wavelengths.[17]

Recent efforts illustrate both progress and limitations. Wang and co-workers[18] reported chiral nanographenes with high Φ_F via helical π-extension of perylene, but emission remained in the visible range (A, Fig. 1a). Chao's[19] "double-twist" pyrene-based nanographenes achieved red-shifted luminescence with moderate Φ_F (~58%), though CPL brightness was modest. Our[20] previous perylene-based helicenes extended emission to 1010 nm, but with enhanced π–π interactions that reduced Φ_F (**B**, Fig. 1a). Similarly, Miao[21] and Jiang[22] expanded perylene diimides into chiral nanographenes with emission spanning the far-red to near-infrared region, yet efficiency

[a] Department of Chemistry, National University of Singapore, 3 Science Drive 3, 117543, Singapore
E-mail: zouya@nus.edu.sg; chmwuj@nus.edu.sg
[b] Shanghai Key Laboratory of Green Chemistry and Chemical Processes, School of Chemistry and Molecular Engineering, East China Normal University, Shanghai 200062, China.
E-mail: hbyang@chem.ecnu.edu.cn
[c] School of Chemistry and Chemical Engineering, Beijing Institute of Technology, Beijing 100081, China.
[#] These authors contributed equally to this work.
† Electronic Supplementary Information (ESI) available. 2491985–2491990. For ESI and crystallographic data in CIF or other electronic format see DOI: 10.1039/x0xx00000x

View Article Online
DOI: 10.1039/D6SC00676K

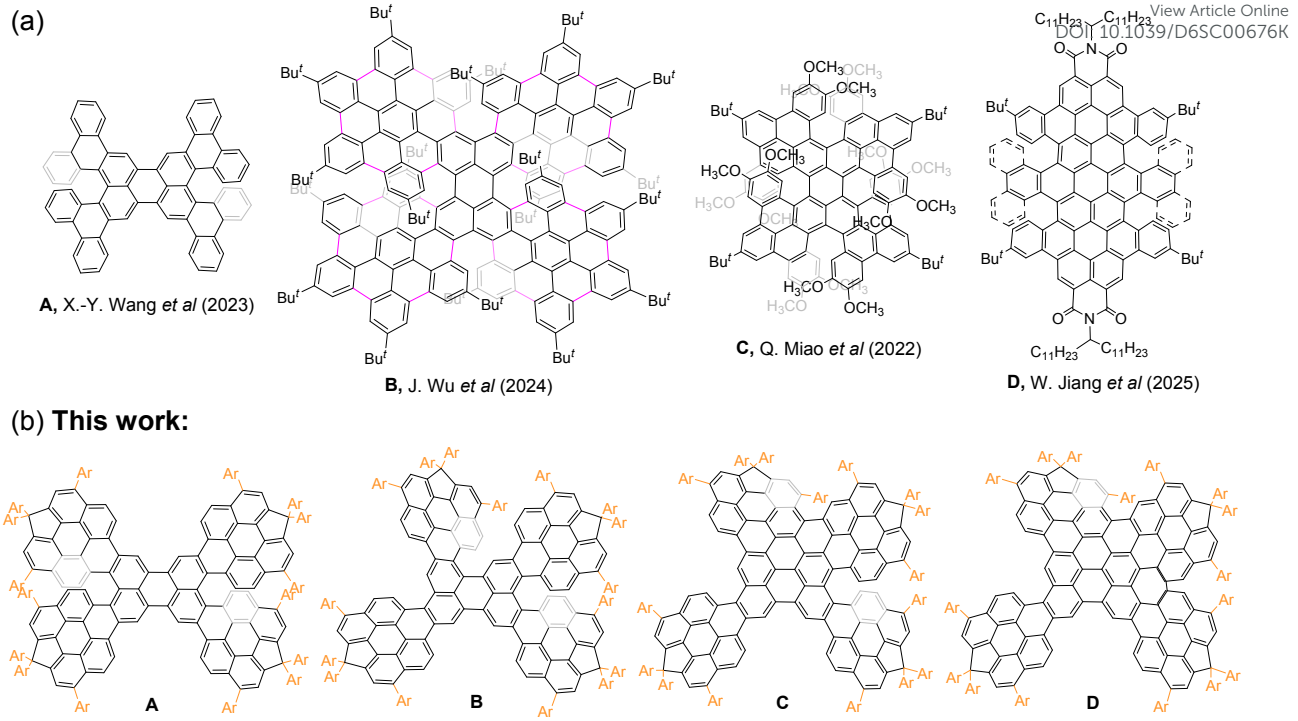

Fig. 1 (a) Representative examples of the reported perylene-embedded chiral nanographene. (b) Novel fused perylene pentamers **1a-d** reported in this work.

losses persisted (**C**-**D**, Fig. 1a). Incorporation of bulky *bay* substituents has been shown to suppress π-aggregation and improve solubility, highlighting a strategy to mitigate ACQ.[23]

These precedents suggest key design principles: π-extension and structural multiplicity enable far red to NIR absorption and emission, molecular rigidity and symmetry reduce nonradiative decay and improve Φ_F, and bulky substituents prevent π-aggregation. Perylene scaffolds are particularly attractive due to high intrinsic fluorescence, favourable frontier molecular orbital (FMO) distributions, and versatile *bay* positions for steric protection.[24] Yet, embedding perylene into extended, rigid architectures while maintaining strong emission and robust CPL remains a major challenge.

Here, we report the synthesis of a series of π-aggregation-free, fused perylene pentamers **1a**-**1d** with butterfly-like architectures that integrate π-extension, structural multiplicity, and steric protection (Fig. 1b). Suzuki coupling and Scholl reactions yield racemic and *meso* isomers, as well as a family of contorted nanographenes confirmed by X-ray crystallography. Bulky aryl substituents and *bay*-fused cyclopentadiene (CP) rings prevent π-aggregation, stabilize enantiomers, and enable efficient chiral HPLC separation. Extended π-conjugation preserves perylene-like FMO distributions, producing emission spanning the far-red to NIR region. Notably, compound **1a-*rac*** exhibits high Φ_F (65%) and B_{CPL} (66.7 M^{-1} cm^{-1}), while **1d** exhibits narrowband emission extending from the far-red into the NIR region. This work demonstrates a generalizable strategy for designing chiral nanographenes that are π-aggregation-free, enantiomerically stable, and tunable in optical and chiroptical properties, achieving simultaneously high fluorescence efficiency and active CPL within a single molecular family.

Result and discussion

Design and synthesis

To access the desired π-aggregation-free, fused perylene pentamers, two modified perylene building blocks, **4** and **5**, were designed and synthesized (Scheme 1). Building block **5**,[25] bearing four pinacol boronate (Bpin) groups, provides a perylene-embedded core for the pentamers and acts as a strongly luminescent chromophore. Building block **4**, a cyclopentadiene-fused perylene featuring sp^3-carbons at one *bay* position, was prepared from compound **2**[26] using a modified protocol. Specifically, compound **2** was coupled with (3,5-di-*tert*-butylphenyl) boronic acid under Suzuki conditions to afford compound **3** in 68% yield. Subsequent bromination of **3** with Br_2 gave building block **4** in 81% yield. The bulky aryl substituents (3,5-di-*tert*-butylphenyl), introduced both at the sp^3-carbons of the fused cyclopentadiene and the *peri* positions, enhance the solubility of **4**, its intermediates, and the final pentamers.

Suzuki coupling between building blocks **4** and **5** yielded a mixture of products **6** and **7** in 23% yield. Compound **6** features a perylene core with a single bulky aryl-substituted perylene unit fused at one *peri*-position. By contrast, compound **7** contains two such units, fused diagonally at the *peri*-positions of the core. Surprisingly, the expected pentamer **8**, in which five perylene units are connected by four C–C single bonds, was not observed (See details in ESI†). Instead, a domino process occurred, generating new C–C bonds *via* an unusual C–H transformation.[27] This unusual reactivity may arise from a palladium-catalyzed C–H activation/C–C cross-coupling pathway, possibly facilitated by the electron-rich, multi-perylene precursor.[28] A possible reaction mechanism is proposed (Fig. S1†). Although the expected product **8** was not obtained under the typical Suzuki coupling conditions, the products **6** and **7** did not affect the subsequent Scholl reaction toward the target fused pentamers.

View Article Online
DOI: 10.1039/D6SC00676K

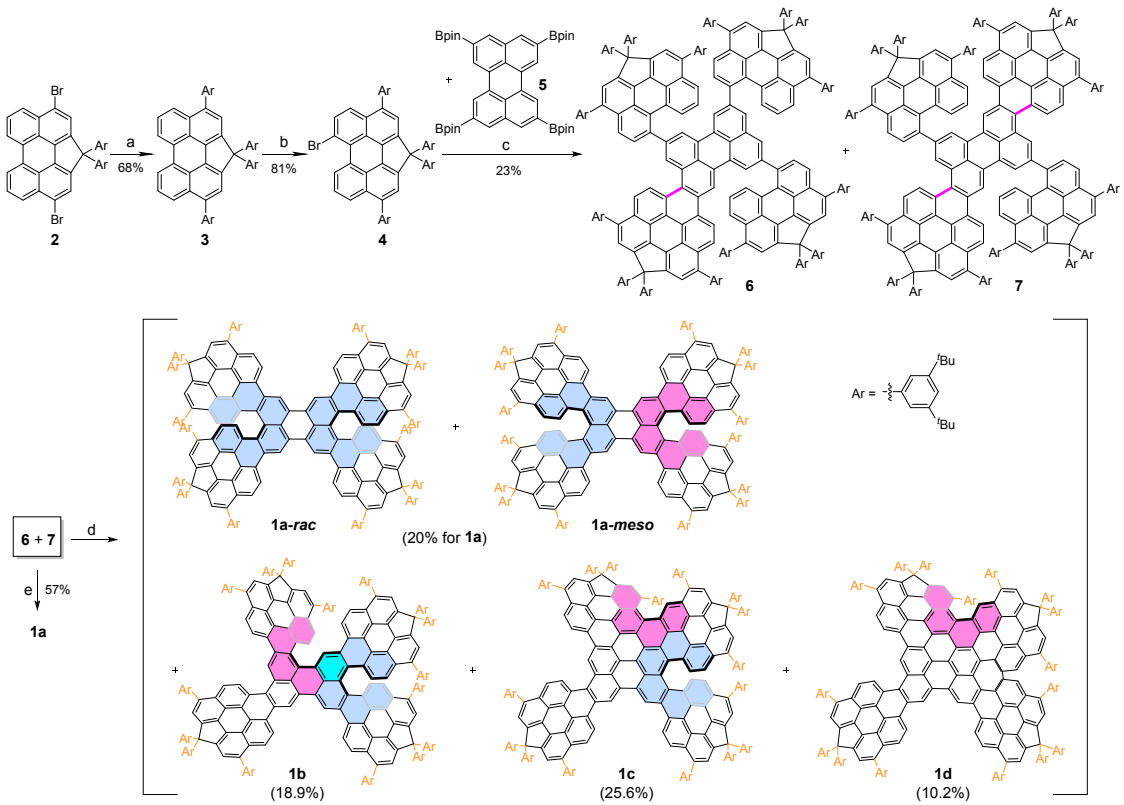

Scheme 1. Synthetic route of compounds **1a-d**. Reaction Conditions: (a) $ArB(OH)_2$ (4.0 eq.), $Pd(dppf)Cl_2{\cdot}CH_2Cl_2$, K_2CO_3, THF/H_2O, 80 °C, overnight; (b) Br_2, DCM, r.t., 1h; (c) $Pd_2(dba)_3{\cdot}CHCl_3$, Sphos, Cs_2CO_3, toluene/H_2O, 90 °C; 32h; (d) DDQ, TfOH, DCM, r.t., 1.5h; (e) $FeCl_3$, $MeNO_2$, DCM, r.t., 1h.

Therefore, no further optimization to obtain **8** was pursued, and compounds **6** and **7** were directly used in the next step.

The final perylene-fused pentamers were obtained *via* the Scholl cyclodehydrogenation reaction,[29] which displayed condition-dependent selectivity. Using DDQ/TfOH, both *peri* and *bay* positions underwent cyclodehydrogenation, yielding a family of tailored pentamers (**1a–1d**) in 10.2–25.6% yields (Scheme 1). Importantly, this method avoided producing a complex mixture of random fusion products, instead, affording structurally defined pentamers (Fig. S34-S35†). In contrast, $FeCl_3$-mediated Scholl reaction induced cyclodehydrogenation exclusively at the *peri* positions, affording pentamer **1a** in 57% yield. Both racemic (**1a-*rac***) and *meso* (**1a-*meso***) isomers were obtained in a nearly 1:1 ratio as determined by ^{1}H NMR (Fig. S10, S66-S71†), whereas diastereomers for **1b–1d** were not observed. These findings highlight the distinct regioselectivity imparted by different Scholl reaction conditions[30] and provide new insights into the construction of molecular nanocarbons.

X-ray crystallographic analysis

The solid-state structures of building block **4**, its precursor **3**, and the intermediate **7** were determined by single-crystal X-ray diffraction (XRD),[31] providing insights into their conformations and packing arrangements (Fig. 2). Single crystals suitable for XRD analysis were obtained through slow solvent diffusion or evaporation. Specifically, crystals of **3** and **7** were grown by slow diffusion of methanol into their chloroform and dichloromethane (DCM) solutions, respectively, while crystals of **4** were obtained by slow vapor diffusion of acetonitrile into its DCM solution. From the side view of **3**, the backbone adopts a nearly planar conformation (Fig. 2a). In contrast, the backbone of **4** exhibits a slightly bent conformation due to the combined effects of the CP ring fused at the *bay* positions and steric hindrance from the bromine substituent at another *bay* position (Fig. 2b). The Br atom at the *bay*-position is oriented outward because of steric repulsion. In both **3** and **4**, the aryl (Ar) groups attached to the *peri* positions and sp^3-carbons orient perpendicularly to the perylene backbone. This orthogonal arrangement of bulky Ar substituents effectively suppresses π–π stacking by occupying the interstitial space between adjacent perylene backbones.

The intermediate **7**, obtained after Suzuki coupling, adopts a butterfly-like conformation (Fig. 2c-2d). The three fused perylene units form a slightly twisted plane, while the two singly linked perylene units lie in another plane, resulting in a cross-shaped arrangement. The Ar groups are distributed around this butterfly-like skeleton and oriented perpendicularly to each connected perylene backbone, thereby creating an environment in which the π-skeleton is effectively encapsulated within the molecule. The distances between the two perylene-based cross planes were measured to be

View Article Online
DOI: 10.1039/D6SC00676K

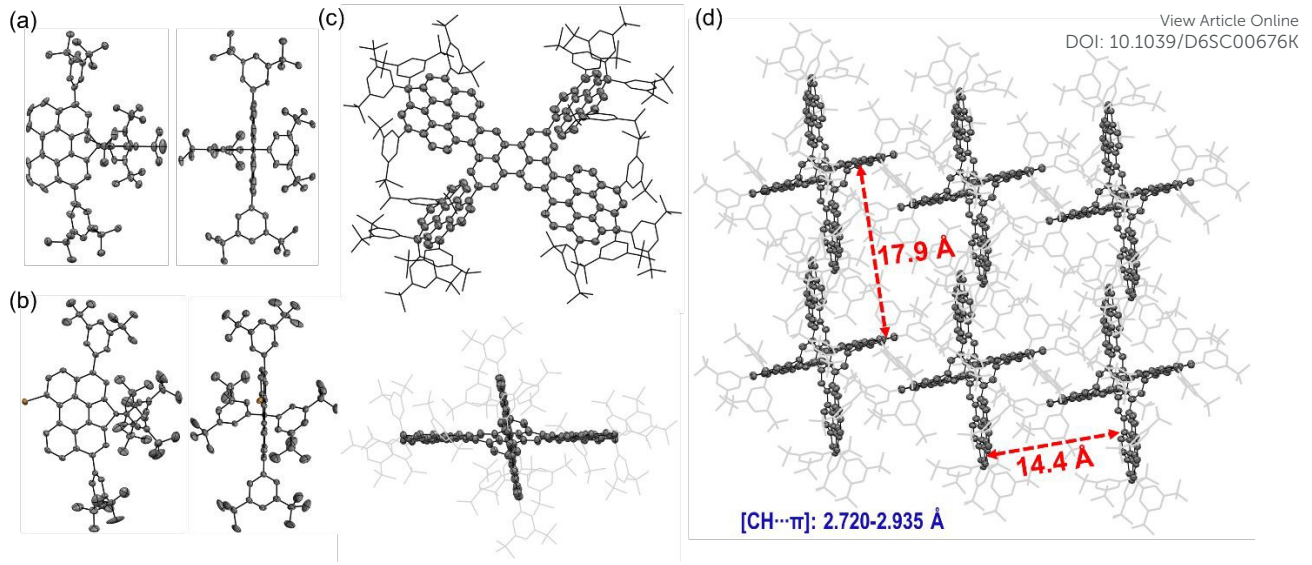

Fig. 2 Top view and side view of X-ray crystallographic structures of (a) **3**, (b) **4** and (c) **7**; (d) molecular packing of X-ray crystallographic structures of **7**.

approximately 17.9 Å and 14.4 Å, respectively—significantly larger than the 3.5 Å separation observed between parent perylene molecules in the solid state.[32] This expanded spacing demonstrates π-aggregation-free crystal packing and highlights the effectiveness of bulky aryl substituents in suppressing π–π aggregation between perylene backbones.

The structures of the final fused perylene pentamers **1a-*meso***, **1b**, and **1c** were unambiguously confirmed by single-crystal X-ray diffraction (Fig. 3).[31] Single crystals of **1a-*meso*** and **1b** were obtained by slow diffusion of methanol into their solutions in *o*-DCB/CS_2 (4:1) and chlorobenzene/CS_2 (3:1), respectively, while crystals of **1c** were grown by slow diffusion of acetonitrile into its toluene/DCM (2:3) solution. Crystals of **1a-*rac*** and **1d** were also obtained but proved too unstable for accurate structure determination, as weak diffraction signals were observed due to solvent loss upon removal from the mother liquor. This instability likely originates from weak intermolecular interactions in the packing, consistent with their pronounced π-aggregation-free behaviour. The possible structures of **1d** are illustrated in Fig. S36. Considering the fusion trend from **1a** to **1c**, together with the C_1 structure confirmed by NMR analysis (Fig. S17–S18 and S75–S76†), structure A in Fig. S36, corresponding to **1d** in Scheme 1, is assigned as the most plausible structure. Furthermore,

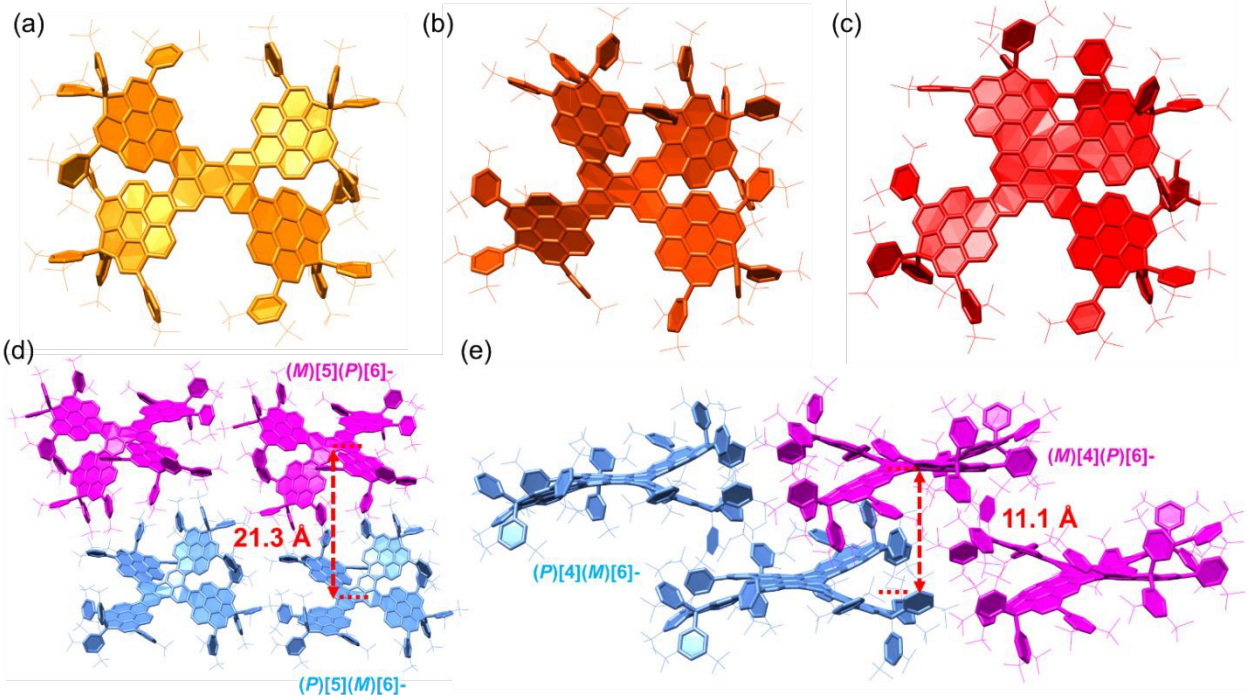

Fig. 3 X-ray crystallographic structures of (a) **1a-*meso***, (b) **1b**, (c) **1c**, and the packing of (d)**1b** and (e) **1c**.

View Article Online
DOI: 10.1039/D6SC00676K

the electronic properties are in good agreement with the calculated results (Fig. 4d, Fig. S28, S48, and S49, and Table S5†), which further supports this assignment.

XRD analysis confirmed the fused perylene pentamer skeletons and butterfly-like geometries of **1a-*meso***, **1b**, and **1c** (Fig. 3). In **1a-*meso***, all aryl-substituted perylene units (Ar–Per) are fused at the *peri*-positions of the perylene (Per) core, generating two extended [6]helicene motifs along opposite sides of the backbone, with bulky substituents distributed around the pentamer framework (Fig. 3a). In **1b**, one Ar–Per unit is fused at a *bay* position rather than a *peri*-position. This structural change gives rise to an extended [6]helicene on the *peri* side and an extended [5]helicene on the *bay* side, while the remaining Ar–Per units maintain the perpendicular orientation relative to the Per backbone, preserving π-aggregation suppression (Fig. 3b, 3d). **1c** builds on the structure of **1b**, incorporating two additional fusions of the Ar–Per unit that forms the [5]helicene in **1b** (Fig. 3c, 3e). Specifically, the *ortho*-position of this Ar–Per unit couples with the *bay* position of the Per core, while its *peri*-position couples with the *ortho*-position of an adjacent Ar–Per unit. These additional fusions enlarge the π-skeleton, forming an extended [6]helicene on the *peri* side and an extended [4]helicene on the *bay* side. The two opposite *peri*-fused Ar–Per units together with the Per core generate a wave-like extended heptacene motif, while on each side, the *bay*-fused Ar–Per unit cooperates with the adjacent *peri*-fused Ar–Per units and the Per core to form stable helical termini, giving rise to *P*[4]*M*[6] or *M*[4]*P*[6] enantiomers. In all three pentamers, the Ar substituents are oriented perpendicular to the Per backbones, consistent with the structures of **3** and **4**. This orthogonal arrangement effectively prevents π–π stacking, thereby minimizing π-aggregation. The crystal packing structures (Fig. 3d-3e; Fig. S51-S61†) further highlight this π-aggregation -free behaviour: the Ar groups occupy the intermolecular spaces around the pentamer backbones, eliminating π–π interactions among the π-conjugated cores.

Enantiomers are equally present in the packing structures of **1b** and **1c**—*P*[5]*M*[6]/*M*[5]*P*[6] for **1b** and *P*[*4*]*M*[6]/*M*[4]*P*[6] for **1c** (Fig. 3d-3e; Fig. S58, S60†). The distances between paired enantiomers are large (21.3 Å for **1b** and 11.1 Å for **1c**), reflecting pronounced non-π-aggregation. Each enantiomeric pair assembles into heterochiral stacked chains in an alternating pattern, predominantly mediated by [CH···π] interactions and van der Waals forces (Fig. S58, S60†). Collectively, these weak intermolecular interactions stabilize the crystals and support the formation of a three-dimensional supramolecular architecture (Fig. S59, S61†).

Photophysical properties

To elucidate the photophysical properties of **1a**–**1d**, their UV–vis–NIR absorption and fluorescence spectra were recorded in dilute DCM solutions (c = 1.0 × 10^{-5} M) at room temperature (Fig. 4). Compared with perylene,[33] all compounds display pronounced red-shifts owing to their extended π-conjugation. For the perylene pentamers **1a-*rac*** and **1a-*meso***, the absorption spectra are nearly identical, with the lowest-energy absorption maxima at 562 nm and 564 nm, respectively, along with a strong absorption band at ~341 nm (Fig. 4a). TD-DFT calculations (Tables S1, S2†) assign the lowest-energy bands to HOMO–LUMO electronic transition. The calculated frontier molecular orbitals (FMOs) of both isomers closely resemble those of perylene (Fig. 4e), and they also display similar absorption maxima (Fig. S38a, S41†).

DFT-calculated energy levels show identical LUMO energies (–2.14 eV) and comparable HOMO energies (–4.60 eV for **1a-*rac*** and –4.56 eV for **1a-*meso***) (Fig. 4e, Fig. S37†, Fig. S40†). Compound **1b** exhibits a markedly red-shifted absorption profile, with a lowest-energy

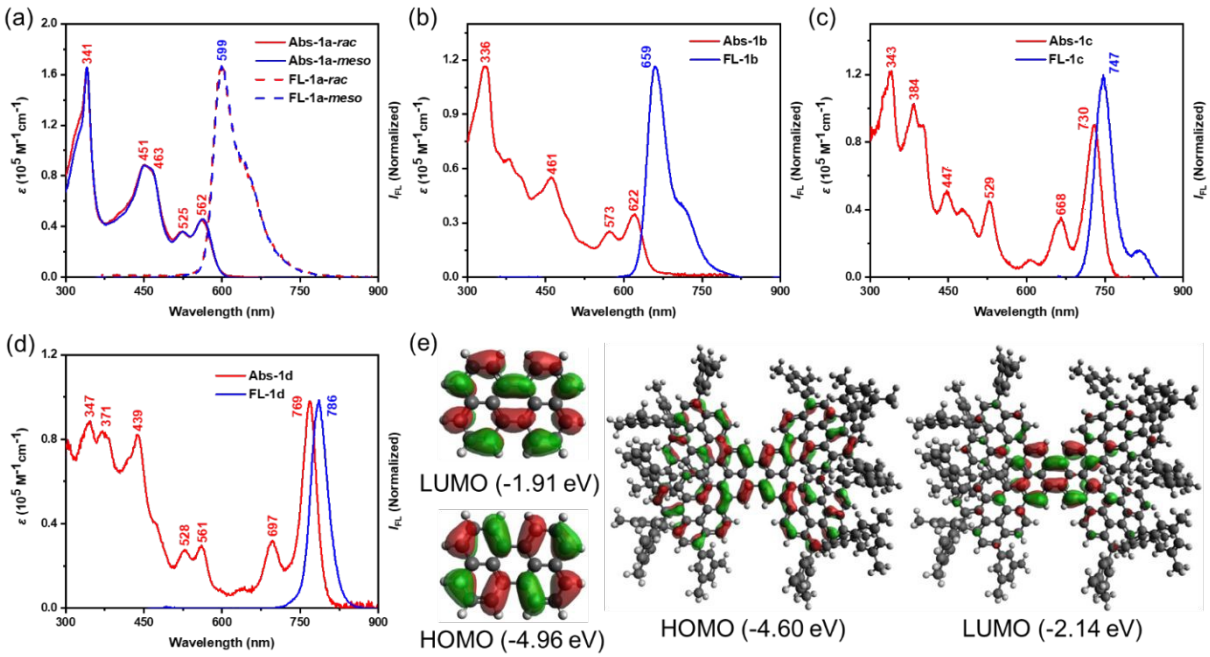

Fig. 4 UV-Vis absorption (Abs) and fluorescence (FL) spectra of (a) **1a-*rac*** and **1a-*meso***, (b) **1b**, (c) **1c**, (d) **1d**; (e) Calculated frontier molecular orbital profiles of perylene and **1a-*rac***. The *tert*-butyl substituents were replaced by methyl groups for the calculations.

View Article Online
DOI: 10.1039/D6SC00675K

maximum at 622 nm extending into the far-red region (Fig. 4b). TD-DFT analysis attributes this band to the HOMO–LUMO transition (Table S3†). The shift arises from the fusion of one Ar–Per unit with the perylene core at the *bay* position rather than the *peri* position, leading to altered electronic structures: a lowered LUMO (–2.28 eV) and a raised HOMO (–4.49 eV) (Fig. S42†). This highlights the critical role of subtle structural changes in tuning electronic properties. Compound **1c** shows an even stronger bathochromic shift, with the lowest-energy maximum at 730 nm and six well-resolved absorption bands at 730, 668, 529, 447, 384 and 345 nm (Fig. 4c). The additional red shift is attributed to further π-extension from two additional fusions, again assigned to the HOMO–LUMO transition by TD-DFT calculations (Table S4†). Compound **1d** exhibits a similar absorption profile to **1c** but with the lowest-energy maximum shifted further to 769 nm, also attributed to a HOMO–LUMO transition (Fig. 4d and Table S5†).

The emission spectra of **1a–1d** were also measured in DCM at room temperature (Fig. 4a-4d), showing trends consistent with the absorption spectra. Compounds **1a-*rac*** and **1a-*meso*** display nearly identical fluorescence spectra with emission maxima at ~599 nm and a broad shoulder extending into the far-red region (Fig. 4a), in line with their similar absorption features and frontier orbital distributions. With the structural modification from *peri*- to *bay*-fusion, **1b** exhibits a red-shifted emission maximum at 659 nm, extending broadly across the visible–NIR range (Fig. 4b). Further π-extension in **1c** leads to a more pronounced shift, with the emission maximum at 747 nm, again spanning a broad spectral window (Fig. 4c). These gradual bathochromic shifts mirror the absorption red-shifts and highlight the sensitivity of the excited-state properties to subtle structural changes. For **1d**, an even larger red shift is observed, with the emission maximum at 786 nm (Fig. 4d). Unlike **1a–1c**, the spectrum of **1d** exhibits narrowband emission extending from the far-red into the NIR region, with negligible visible-region contributions or shoulder peaks, reflecting its more extended π-conjugation and distinct helical framework. It is worth noting that these π-extended systems exhibit a certain sensitivity to light and thermal conditions (Fig. S21†). Weak additional signals may appear on the high-energy side of the emission spectra upon exposure to ambient light or thermal treatment. These features are fully suppressed under strict exclusion of light and thermal input. This observation highlights the importance of careful control of light and temperature during spectroscopic measurements of large π-conjugated systems.

The absolute fluorescence quantum yields (Φ_F) of **1a–1d**, determined using an integrating sphere, are 65% (**1a-*rac***), 59% (**1a-*meso***), 24% (**1b**), and 7% (**1c**, **1d**). These values reveal a general decrease in Φ_F as emission moves into the far-red to NIR region, consistent with the energy gap law,[34] where smaller energy gaps enhance non-radiative decay through vibronic coupling. Nevertheless, compounds **1a–c** maintain relatively high Φ_F

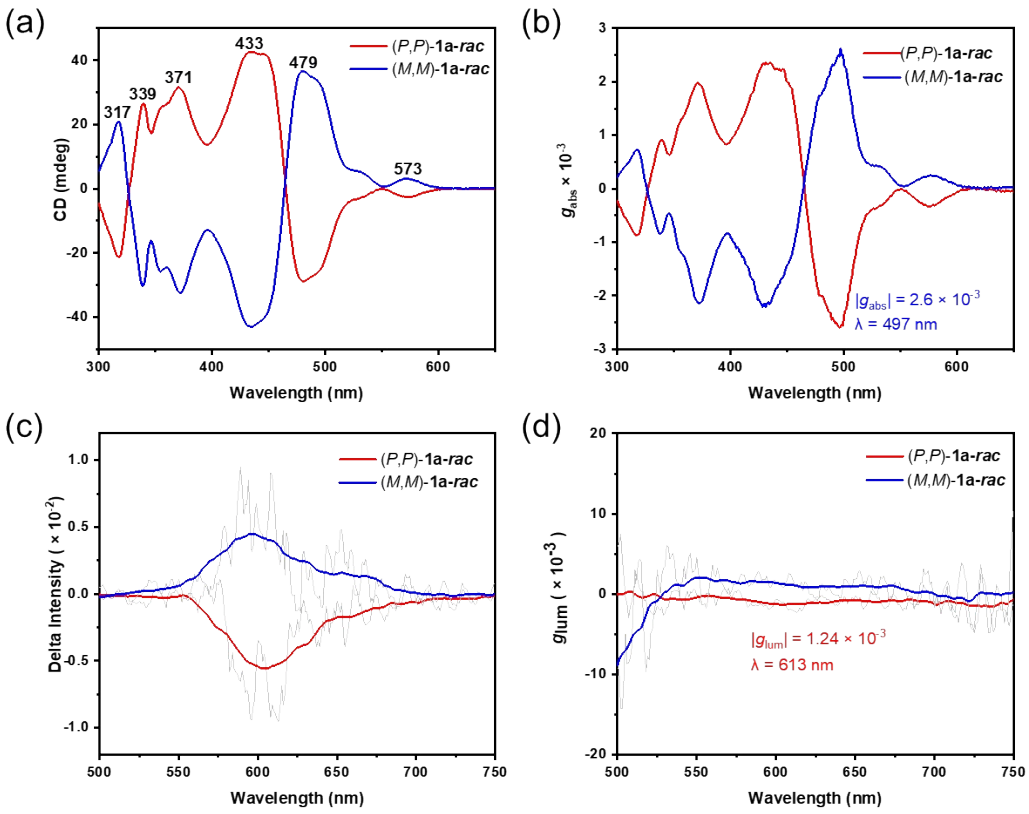

Fig. 5 (a-b) Circular dichroism spectra of the enantiomers of **1a-*rac*** measured in DCM. (c-d) Circularly polarized luminescence (CPL) spectra of enantiomers of **1a-*rac*** in DCM (*c*: 1.2 × 10^{-5} M); the light gray line shows the original, unsmoothed data.

View Article Online
DOI: 10.1039/D5SC00675K

compared to other nanographenes with far-red to NIR emission,[35] while **1d** is noteworthy as a rare helical nanographene exhibiting narrowband emission spanning the far-red to NIR region with a full width at half maximum (FWHM) of 37 nm (compared to 70 nm for **1a-*rac***, 43 nm for **1b** and 42 nm for **1c**) and a respectable Φ_F of 7%, surpassing some molecular nanocarbon–based far-red to NIR fluorophores.[36]

Time-resolved fluorescence measurements reveal a clear trend of faster decay with increasing π-extension: the lifetimes decrease from 6.3 ns (**1a-*rac***) and 6.2 ns (**1a-*meso***) to 4.3 ns (**1b**) and 3.3 ns (**1c**), with **1d** showing a slightly longer lifetime of 3.9 ns (Fig. S19†). In parallel, the FWHM narrow progressively from 70 nm (**1a**) to 37 nm (**1d**), indicating increasingly well-defined emission profiles. This trend can be attributed to the enhanced structural rigidity and reduced conformational freedom associated with extended π-conjugation and fused frameworks. The increased rigidity suppresses vibronic coupling and limits excited-state geometric relaxation, thereby diminishing vibronic sidebands and resulting in narrower emission bands with improved spectral purity.[37] These observations demonstrate how subtle variations in fusion topology and π-extension govern excited-state relaxation dynamics, thereby modulating both the efficiency and spectral purity of the emission.

Taken together with the absorption analysis, these results demonstrate that while the perylene pentamers share a common backbone, subtle isomeric variations and π-extension induce profound changes in their photophysical behaviour. The lowest-energy absorption and emission bands shift from 562/599 nm in **1a** to 769/786 nm in **1d**, corresponding to red shifts of 207 nm and 187 nm, respectively, accompanied by significant narrowing of emission bandwidth.

Chiral properties

Successful chiral resolution of the perylene pentamers was achieved by chiral HPLC using an acetone/THF mixture as the eluent, affording enantiomerically pure **1a-*rac*** and **1b–1d** (Fig. S22–S28†). Owing to the rigid π-conjugated frameworks and the steric shielding from peripheral aryl groups, no racemization was observed even after 30 days at room temperature, confirming their exceptional configurational stability and high racemization barriers. The absolute configurations of the *P*- and *M*-enantiomers were assigned by comparing the experimental and simulated circular dichroism (CD) spectra. The CD spectra recorded in DCM (Fig. 5, Fig. S26–S28†) exhibit perfectly mirror-symmetric Cotton effects (CEs) over 300–800 nm for each enantiomeric pair. For instance, (*P*,*P*)-**1a-*rac*** displays a first positive CE at 339 nm and a first negative CE at 317 nm (Fig. 5a), followed by additional positive bands at 371 nm and 433 nm, and negative bands at 479 nm and 573nm, while its (*M*,*M*)-counterpart shows exact mirror symmetry. The simulated CD profiles reproduce both the sign and intensity of the experimental features, validating

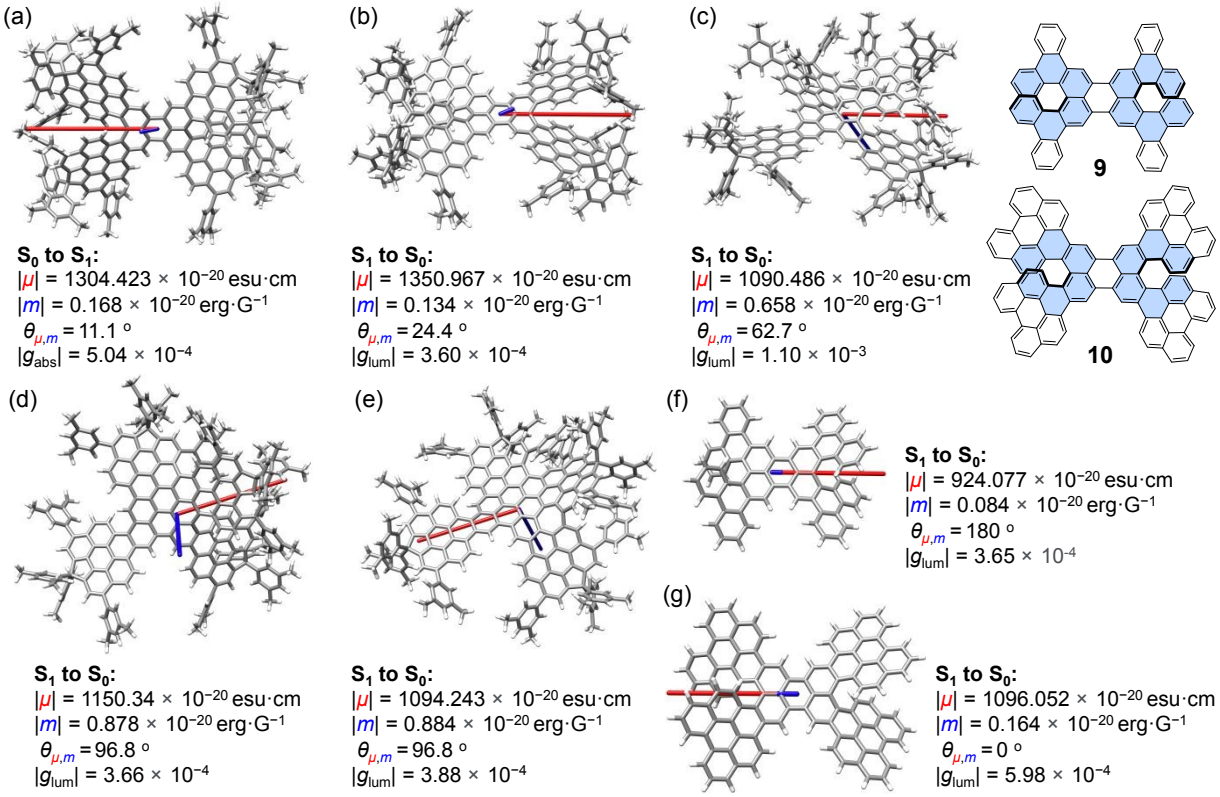

Fig. 6 Calculated transition dipole moments for (a) S_0 to S_7 of **1a-*rac***; and S_1 to S_0 electronic transitions of **1a-*rac*** (b), **1b** (c), **1c** (d), **1d** (e), **9** (f) and **10** (g). The μ vector is shown in red, and the *m* vector is shown in blue. The length of the μ vector is reduced 100 times when the length of the *m* vector is amplified 10 times for clarity. Calculated by TD-DFT at the B3LYP-D3-6-31G(d,p) level.

the configuration assignments and confirming the high chiroptical purity of all enantiomers. Across the series **1a–1d**, the CD spectra exhibit a systematic bathochromic shift of the lowest-energy Cotton effect, consistent with progressive π-extension and fusion topology modification, which mirrors the red-shift observed in the UV–vis absorption spectra. In particular, the chiroptical response gradually extends from the UV region (**1a**) toward the far-red region (**1d**), indicating effective modulation of electronic transitions through structural engineering (Fig. 5a, Fig. S26–S28†). The absorption dissymmetry factors ($|g_{abs}|$) were derived from the CD spectra, revealing that both the magnitude and wavelength of the maxima can be tuned systematically by subtle isomeric variation and π-extension. The maximum $|g_{abs}|$ values were determined to be 0.0026 at 497 nm (**1a-*rac***)**,** 0.0023 at 498 nm (**1b**)**,** 0.0024 at 444 nm (**1c**), and 0.0042 at 594 nm (**1d**) (Fig. 5b, Fig. S26-28†), indicating that progressive π-extension and topology modification effectively shift the chiroptical response from the UV–vis to the far-red region while enhancing $|g_{abs}|$ in the extended system. The CPL spectra of the enantiopure compounds **1a-*rac*** recorded in DCM (Fig. 5c-5d) display characteristic mirror-image profiles corresponding to its fluorescence spectra. The (*P*,*P*)- and (*M*,*M*)-**1a-*rac*** pair show distinct CPL signals with a maximum $|g_{lum}|$ of 1.24×10^{-3} at 613 nm. The CPL spectra of **1b–1d** were also measured in DCM, but exhibit very weaker CPL responses due to their emission extending into the far-red to NIR region, where reduced energy gaps lead to decreased radiative efficiency and consequently attenuated CPL intensity, in accordance with the energy-gap law.

To comprehensively assess CPL performance, the brightness of CPL (B_{CPL}) was estimated using $B_{CPL} = \varepsilon \times \Phi \times |g_{lum}| / 2$,[10] where ε is the molar extinction coefficient at the excitation wavelength. For **1a-*rac***, the calculated B_{CPL} value is 66.7 M^{-1} cm^{-1}, representing a significant improvement over compound **9**[18] (32 M^{-1} cm^{-1}) and our previously reported perylene-based chiral nanographene[20] (**B**, Fig. 1a), whose CPL signal was too weak to yield a reliable g_{lum} value. This enhancement is primarily attributed to the high molar absorptivity (ε = 165,420 M^{-1} cm^{-1} at 341 nm) resulting from the larger π-extension, highlighting the crucial role of π-expansion in strengthening chiroptical properties. In addition, the improved rigidity and symmetry of the unique fused perylene pentamer skeleton further contribute to the boosted CPL performance. The B_{CPL} value of **1a-*rac*** therefore reflects an efficient balance between absorption strength, emission efficiency, and chiroptical activity, underscoring the importance of π-extension and structural rigidity in enhancing CPL performance.

Theoretical analysis

To elucidate the origins of the experimental $|g_{abs}|$ and $|g_{lum}|$ values, transition dipole moment (TDM) calculations were performed for the key absorption and emission transitions (Fig. 6). The dissymmetry factor can be expressed as $g = 4\cos\vartheta\ |m|\ |\mu| / (|m|^2 + |\mu|^2)$, where μ and m are the electric and magnetic transition dipole moments, and ϑ is the angle between them.[38] For **1a-*rac***, the $S_0 \rightarrow S_1$transition shows ϑ = 11.1°, corresponding to nearly parallel alignment of μ and m, an outcome of its D_2-symmetric, X-shaped π-skeleton (Fig. 6a), while the higher-energy $S_0 \rightarrow S_7$ transition responsible for the maximum $|g_{abs}|$ exhibits ϑ = 175°, indicating an almost antiparallel orientation of μ and m (Fig. S50†). Compared with the $S_0 \rightarrow S_1$ transition of **1a-*rac***, the emissive $S_1 \rightarrow S_0$ transition shows ϑ = 24.4°, suggesting a partial loss of ideal symmetry in the excited state (Fig. 6b). For **1b–1d**, the ground-state symmetry is reduced to C_1, and the calculated μ–m angles for $S_1 \rightarrow S_0$ transitions increase to 62.7°, 96.8°, and 96.8°, respectively (Fig. 6c-6e). Despite these larger angles, the calculated $|g_{lum}|$ values are higher than that of **1a-*rac***. This apparent paradox arises from their smaller $|\mu|$ and larger $|m|$, yielding higher $|m|$ / $|\mu|$ ratios, which dominate g according to the simplified expression $g = 4\cos\vartheta\ |m| / |\mu|$.[20] Thus, fine-tuning the relative magnitudes of m and μ through isomeric topology control emerges as a critical strategy for optimizing chiroptical performance.

Comparative calculations for reference systems **9** and **10** further reinforce this design principle (Fig. 6f-6g). Upon π-extension of the conjugated framework, both $|\mu|$ and $|m|$ increase, but the enhancement in $|m|$ is more pronounced, leading to a larger $|g_{lum}|$ for **10**, despite its retention of D_2 symmetry in both ground and excited states. Conversely, the aryl substituents in **1a-*rac*** act as electron-donating groups, increasing $|\mu|$ and thus reducing the $|m|$ / $|\mu|$ ratio, accounting for its smaller $|g_{lum}|$.[39] These insights highlight that while molecular symmetry is a key determinant of the μ–m alignment,[40] electronic substituent effects and π-extension can modulate the balance between electric and magnetic contributions more effectively.

The chiroptical study reveals a clear structure–property relationship: (1) π-extension progressively red-shifts CD into the far-red region and emission into the far-red to near-infrared region, (2) $|g_{abs}|$ and $|g_{lum}|$ are governed by the $|m|$ / $|\mu|$ ratio rather than symmetry alone, and (3) maintaining high Φ_F and radiative efficiency remains essential for maximizing observable CPL brightness. These results offer molecular-level understanding of how topological variation, conjugation length, and symmetry interplay to dictate the chiroptical responses of helical nanographenes.

Conclusions

In summary, a series of fully π-conjugated butterfly-like fused perylene pentamers (**1a–1d**) with well-defined topological variations were successfully synthesized through a C–H transformation followed by a selective Scholl reaction, enabling systematic modulation of their photophysical and chiroptical properties. The rigid, helically twisted nanographene skeletons endow these compounds with exceptional configurational stability and strong absorption spanning from the UV–vis to the far-red to NIR region. Subtle isomeric variations and π-extension effectively tune their fluorescence color, quantum yield, and emission bandwidth, leading to a high quantum yield of up to 65% and narrowband emission spanning the far-red to NIR region with a FWHM of 37 nm. These results reveal a clear structure–property correlation governed by conjugation length and backbone symmetry.

Comprehensive studies of chiroptical properties further demonstrate that both the magnitude and spectral position of $|g_{abs}|$ and $|g_{lum}|$ can be precisely controlled by molecular topology. Transition dipole moment analyses reveal that the dissymmetry factors are predominantly governed by the balance between electric and magnetic transition dipole moments ($|m|$ / $|\mu|$ ratio) rather than symmetry alone. Notably, **1a-*rac*** achieves outstanding CPL

brightness (66.7 M^{-1} cm^{-1}) among nanographene emitters, highlighting the strong interplay between π-extension, electronic substitution, and radiative efficiency.

Overall, this integrated investigation of photophysical and chiroptical behaviors establishes a unified molecular design strategy for next-generation CPL emitters. By jointly optimizing conjugation topology, substituent electronics, and molecular symmetry, these findings pave the way toward high-brightness, CPL-active chiral nanographenes for advanced optoelectronic, sensing, and bioimaging applications.

Author Contributions

J. W., H.-B. Y. and Y. Z. supervised the project. Q. Z. synthesized and characterized the compounds. Z. S. and Z. Y. synthesized the starting materials. R. L., L. J. and W. F performed crystallographic analysis. Q. Z. performed HPLC analysis. L.-T. B. performed circular dichroism and circularly polarized luminescence measurements. Q. Z. and R. L. carried out the calculations. All authors discussed the results and contributed to the manuscript writing.

Conflicts of interest

There are no conflicts to declare.

Acknowledgements

J. W. and Y. Z. acknowledge financial support from the A*STAR MTC IRG/YIRG projects (M22K2c0083 and M22K3c0095) and the MOE Tier 3 program (MOET32024-0002)). H.-B.Y. acknowledges the financial support sponsored by the NSFC (92056203) and Shanghai Frontiers Science Center of Molecule Intelligent Syntheses. We also extend our thanks to Prof. Donglin Jiang and Dr. Yongzhi Chen at NUS, for their assistance with absolute fluorescence quantum yield and fluorescence lifetime measurements.

Notes and references

1 (a) L. Zhang, H.-X. Wang, S. Li, M. Liu, *Chem. Soc. Rev.*, 2020, **49**, 9095–9120; (b) H. V. Anderson, N. D. Gois, W. A. Chalifoux, *Org. Chem. Front.*, 2023, **10**, 4167–4197; (c) V. Kumar, J. L. Páez, S. Míguez-Lago, J. M. Cuerva, C. M. Cruz, A. G. Campaña, *Chem. Soc. Rev.*, 2025, **54**, 4922–4947; (d) N. Liang, D. Meng, Z. Wang, *Acc. Chem. Res.*, 2021, **54**, 961–975; (e) M. Ball, Y. Zhong, Y. Wu, C. Schenck, F. Ng, M. Steigerwald, S. Xiao, C. Nuckolls, *Acc. Chem. Res.*, 2015, **48**, 267–276; (f) J. M. Fernández-García, P. J. Evans, S. Filippone, M. Á. Herranz, N. Martín, *Acc. Chem. Res.*, 2019, **52**, 1565-1574; (g) Y. Zhang, S. H. Pun, Q. Miao, *Chem. Rev.*, 2022, **122**, 14554–14593; (h) Y. Zhu, J. Wang, *Acc. Chem. Res.*, 2023, **56**, 363-373; (i) Z. Gan, J. Lai, L. Lai, S.-Y. Xie, Q. Zhang, *Adv. Optical Mater.*, 2025, **13**, e00976.

2 (a) D. Kuck, *Chem. Rev.*, 2006, **106**, 4885–4925; (b) Y. Zhu, Z. Xia, Z. Cai, Z. Yuan, N. Jiang, T. Li, Y. Wang, X. Guo, Z. Li, S. Ma, D. Zhong, Y. Li, J. Wang, *J. Am. Chem. Soc.*, 2018, **140**, 4222–4226; (c) X. Liu, Z. Jin, F. Qiu, Y. Guo, Y. Chen, Z. Sun, L. Zhang, *Angew. Chem. Int. Ed.*, 2024, **63**, e202407547.

3 (a) L. Zhang, I. Song, J. Ahn, M. Han, M. Linares, M. Surin, H.-J. Zhang, J. H. Oh, J. Lin, *Nat. Commun.*, 2021, **12**, 142; (b) X. -Y. Wang, X. -C. Wang, A. Narita, M. Wagner, X. -Y. Cao, X. Feng, K. Müllen, *J. Am. Chem. Soc.*, 2016, **138**, 12783-12786; (c) C. M. Cruz, S. Castro-Fernández, E. Maçôas, J. M. Cuerva, A. G. Campaña, *Angew. Chem. Int. Ed.*, 2018, **57**, 14782-14786; (d) C. M. Cruz, I. R. Márquez, S. CastroFernández, J. M. Cuerva, E. Maçôas, A. G. Campaña, *Angew. Chem. Int. Ed.*, 2019, **58**, 8068-8072; (e) S. Ma, J. Gu, C. Lin, Z. Luo, Y. Zhu, J. Wang, *J. Am. Chem. Soc.*, 2020, **142**, 16887-16893; (f) M. A. Medel, R. Tapia, V. Blanco, D. Miguel, S. P. Morcillo, A. G. Campaña, *Angew. Chem. Int. Ed.*, 2021, **60**, 6094-6100; (g) W. Niu, Y. Fu, Z. -L. Qiu, C. J. Schürmann, S. Obermann, F. Liu, A. A. Popov, H. Komber, J. Ma, X. Feng, *J. Am. Chem. Soc.*, 2023, **145**, 26824-26832; (h) P. Izquierdo-García, J. M. Fernández-García, S. Medina Rivero, M. Šámal, J. Rybáček, L. Bed-nárová, S. RamírezBarroso, F. J. Ramírez, R. Rodríguez, J. Perles, D. García-Fresnadillo, J. Crassous, J. Casado, I. G. Stará, N. Martín, *J. Am. Chem. Soc.*, 2023, **145**, 11599-11610; (i) Y.-Y. Ju, L. Chai, K. Li, J.-F. Xing, X.-H. Ma, Z.-L. Qiu, X.-J. Zhao, J. Zhu, Y.-Z. Tan, *J. Am. Chem. Soc.*, 2023, **145**, 2815-2821; (j) F. Morita, Y. Kishida, Y. Sato, H. Sugiyama, M. Abekura, J. Nogami, N. Toriumi, Y. Nagashima, T. Kinoshita, G. Fukuhara, M. Uchiyama, H. Uekusa, K. Tanaka, *Nat. Synth.*, 2024, *3*, 774-786; (k) Z. Gan, Z.-C. Chen, H.-R. Tian, G.-C. Yuan, Y.-F. Wu, J. Li, M.-L. Zhang, S.-L. Deng, Q. Zhang, S.-Y. Xie, *Angew. Chem. Int. Ed.*, 2025, **64**, e21600; (l) Y.-Y. Ju, J.-F. Xing, Y.-M. Xie, X.-F. Li, X.-J. Zhao, G.-H. Nie, B. Zhang, Y.-Z. Tan, *J. Am. Chem. Soc.*, 2025, **147**, 45514–45522; (m) W. Liu, H. Zhang, T. Zhang, Z. Lu, Y. Wagenhäuser, F. Würthner, C. Zhu, *Angew. Chem. Int. Ed.*, 2026, **65**, e5649022; (n) K. Zhang, Z.-C. Chen, Y.-F. Wu, H.-R. Tian, L. Zhang, M.-L. Zhang, S.-L. Deng, Q. Zhang, S.-Y. Xie, L.-S. Zheng, *Angew. Chem. Int. Ed.*, 2024, **63**, e202417269.

4 X. Wu, X. Yan, Y. Chen, W. Zhu, P.-T. Chou, *Trends Chem.*, 2023, **5**, 734–747.

5 (a) C. Kulkarni, A. K. Mondal, T. K. Das, G. Grinbom, F. Tassinari, M. F. J. Mabesoone, E. W. Meijer, R. Naaman, *Adv. Mater.*, 2020, **32**, 1904965; (b) V. Kiran, S. P. Mathew, S. R. Cohen, I. Hernández Delgado, J. Lacour, R. Naaman, *Adv. Mater.*, 2016, **28**, 1957-1962.

6 J. G. Ibanez, M. E. Rincón, S. Gutierrez-Granados, M. h Chahma, O. A. Jaramillo-Quintero, B. A. Frontana-Uribe, *Chem. Rev.*, 2018, **118**, 4731–4816.

7 (a) P. Izquierdo-García, J. M. Fernández-García, I. Fernández, J. Perles, N. Martín, *J. Am. Chem. Soc.*, 2021, **143**, 11864–11870; (b) Y.-F. Wu, S.-W. Ying, S.-D. Liao, L. Zhang, J.-J. Du, B.-W. Chen, H.-R. Tian, F.-F. Xie, H. Xu, S.-L. Deng, Q. Zhang, S.-Y. Xie, L.-S. Zheng, *Angew. Chem. Int. Ed.*, 2022, **61**, e202204334; (c) J. Wang, C. Shen, G. Zhang, F. Gan, Y. Ding, H. Qiu, *Angew. Chem. Int. Ed.*, 2022, **61**, e202115979; (d) S. Li, R. Li, Y. K. Zhang, S. Wang, B. Ma, B. Zhang and P. An, *Chem. Sci.*, 2023, **14**, 3286–3292; (e) R. Li, B. Ma, S. Li, C. Lu, P. An, *Chem. Sci.*, 2023, **14**, 8905–8913; (f) W. Niu, Y. Fu, Q. Deng, Z. L. Qiu, F. Liu, A. A. Popov, H. Komber, J. Ma, X. Feng, *Angew. Chem. Int. Ed.*, 2024, **63**, e202319874; (g) Y. Ma, L. Zhou, J. Tan, W. Sun, Y. Zou and Y. Hu, *Adv. Opt. Mater.*, 2025, **13**, 2402446; (h) X. Wang, J. Bai, Y. Shen, Z. Li and H. Gong, *Angew. Chem. Int. Ed.*, 2025, **64**, e202417745; (i) Y.-Y. Ju, L.-E. Xie, J.-F. Xing, Q.-S. Deng, X.-W. Chen, L.-X. Huang, G.-H. Nie, Y.-Z. Tan, B. Zhang, *Angew. Chem. Int. Ed.*, 2025, **64**, e202414383; (j) P. Izquierdo-García, J. M. Fernández-García, J. Perles, I. Fernández, N. Martín, *Angew. Chem. Int. Ed.*, 2023, **62**, e202215655; (k) Z. Qiu, C. W. Ju, L. Frédéric, Y. Hu, D. Schollmeyer, G. Pieters, K. Müllen, A. Narita, *J. Am. Chem. Soc.*, 2021, **143**, 4661–4667;(l) C. M. Cruz, I. R. Márquez, I. F. A. Mariz, V. Blanco, C. Sánchez-Sánchez, J. M. Sobrado, J. A. Martín-Gago, J. M. Cuerva, E. Maçôas and A. G. Campaña, *Chem. Sci.*, 2018, **9**, 3917–3924; (m) R. Li, D. Wang, S. Li, P. An, *Beilstein J. Org. Chem.*, 2023, **19**, 736–751; (n) K. M. Cheung, Y. Xiong, S. H. Pun, X. Zhuo, Q. Gong, X. Zeng, S. Su, Q. Miao, *Chem*,2023, **9**, 2855–2868; (o) W. Jiang, Z. Wang, *J. Am. Chem. Soc.*, 2022, **144**, 14976–14991.

8 (a) Z. Qiu, S. Asako, Y. Hu, C.-W. Ju, T. Liu, L. Rondin, D. Schollmeyer, J. S. Lauret, K. Müllen, A. Narita, *J. Am. Chem. Soc.*, 2020, **142**, 14814–14819; (b) H. Shi, B. Xiong, Y. Chen, C. Lin, J. Gu, Y. Zhu, J. Wang, *Chin. Chem. Lett.*, 2023, **34**, 107520; (c) Y. Zhu, X. Guo, Y. Li, J. Wang, *J. Am. Chem. Soc.*, 2019, **141**, 5511–5517; (c) X. Xu, R. M. Mármol, S. Vasylevskyi, A. Villa, G. Folpini, F. Scotognella, G. M. Paternò, A. Narita, *Angew. Chem. Int. Ed*., 2023, **62**, e202218350; (d) Y.-J. Shen, N.-T. Yao, L.-N. Diao, Y. Yang, X.-L. Chen, H.-Y. Gong, *Angew. Chem. Int. Ed*., 2023, **62**, e202300840; (e) J. Liu, T. He, Z.-L. Gong, N. Liang, Y. Feng, G. Long, Y.-W. Zhong, C.-J. Yao, *Adv. Optical Mater*., **2023**, **12**, 2302486; (f) X. Tian, K. Shoyama, B. Mahlmeister, F. Brust, M. Stolte, F. Würthner, *J. Am. Chem. Soc.*, 2023, **145**, 9886–9894; (g) X. Xiao, S. K. Pedersen, D. Aranda, J. Yang, R. A. Wiscons, M. Pittelkow, M. L. Steigerwald, F. Santoro, N. J. Schuster, C. Nuckolls, *J. Am. Chem. Soc*., 2021, **143**, 983−991; (h) J. Tan, X. Xu, J. Liu, S. Vasylevskyi, Z. Lin, R. Kabe, Y. Zou, K. Müllen, A. Narita, Y. Hu, *Angew. Chem. Int. Ed.*, 2023, **62**, e202218494.

9 G.-F. Huo, Y. Han, W. Fan, Y. Zou, J. Wu, *Chem Asian J*., 2025, **20**, e00442.

10 L. Arrico, L. Di Bari, F. Zinna, *Chem. Eur. J*., 2021, **27**, 2920–2934.

11 (a) H. Tanaka, Y. Inoue, T. Mori, *ChemPhotoChem*, 2018, **2**, 386–402; (b) G. Albano, G. Pescitelli, L. Di Bari, *Chem. Rev*., 2020, **120**, 10145−10243; (c) Y. Nagata, T. Mori, *Front. Chem*., 2020, **8**, 448–453; (d) T. Mori, *Chem. Rev*., 2021, **121**, 2373−2412.

12 Z.-A. Li, K.-L. Zhu, J. Liang, H.-Y. Gong, *Aggregate*, 2025, e70147.

13 (a) Y. Zhang, J. Guan, L. Luo, X. Han, J. Wang, Y. Zheng, J. Xu, *Interd. Mater*., 2024, **3**, 453–479; (b) W. Niu, Y. Fu, Z.-L. Qiu, C. J. Schürmann, S. Obermann, F. Liu, A. A. Popov, H. Komber, J. Ma, X. Feng, *J. Am. Chem. Soc.*, 2023, **145**, 26824−26832; (c) A. Tsurusaki, K. Kamikawa, *Chem. Lett.*, 2021, **50**, 1913–1932; (d) C. Li, Y. Yang, Q. Miao, *Chem. Asian J.*, 2018, **13**,884 –894; (e) W.-B. Lin, M. Li, L,Fang, C.-F. Chen, *Chin. Chem. Lett.*, 2018, **29**, 40–46.

14 R. Weissleder, *Nat. Rev. Cancer*, 2002, **2**, 11–18.

15 D. Zhu, W. Jiang, Z. Ma, J. Feng, X. Zhan, C. Lu, J. Liu, J. Liu, Y. Hu, D. Wang, Y. S. Zhao, J. Wang, Z. Wang, L. Jiang, *Nat. Commun*., 2022, **13**, 3454.

16 (a) N. Liang, C. Cao, Z. Xie, J. Liu, Y. Feng, C.-J. Yao, *Mater. Today*, 2024, **75**, 309–333; (b) D. Dini, M. J. F. Calvete, M. Hanack, *Chem. Rev*., 2016, **116**, 13043-13233; (c) S. MíguezLago, I. F. A. Mariz, M. A. Medel,J. M. Cuerva, E. Maçôas, C. M. Cruz, A. G. Campaña, *Chem. Sci.*, 2022, **13**, 10267-1027.

17 Y.-C. Tsai, Y.-C. Chen, H.-F. Lu, K.-M. Chan, S.-L. Lin, P.-X. Lin, R. Rotomskis, S. Steponkiene, T.-K. Wu, M.-H. Chan, J. A. Ho, Y.-F. Huang, C.-P. Hsu, Y.-H. Chan, *J. Am. Chem. Soc*., 2025, **147**, 21940−21949.

18 J.-K. Li, X.-Y. Chen, W.-L. Zhao, Y.-L. Guo, Y. Zhang, X.-C. Wang, A. C.-H. Sue, X.-Y. Cao, M. Li, C.-F. Chen, X.-Y. Wang, *Angew. Chem. Int. Ed.*, 2023, **62**, e202215367.

19 Y. Dong, Z. Zhang, Y. Hashikawa, H. Meng, F. Bai, K. Itami, Chaolumen, *Angew. Chem. Int. Ed.*, 2024, **63**, e202406927.

20 G.-F. Huo, W.-T. Xu, Y. Han, J. Zhu, X. Hou, W. Fan, Y. Ni, S. Wu, H.-B. Yang, J. Wu, *Angew. Chem. Int. Ed.*, 2024, **63**, e202403149.

21 S. H. Pun, K. M. Cheung, D. Yang, H. Chen, Y. Wang, S. V. Kershaw, Q. Miao, *Angew. Chem. Int. Ed.*, 2022, **61**, e202113203.

22 Y. Zhao, Z. Liu, X. Wen, K. Chen, G. Liu, Z. Wang, W. Jiang, *Angew. Chem. Int. Ed.*, 2025, **64**, e202507891.

23 L. Jiao, Y. Zou, W. Fan, Y. Han, Q. Zhou, J. Shao, J. Wu, *J. Am. Chem. Soc.*, 2025, **147**, 9415-9423.

24 M. Giordano, F. Cardano, C. Barolo, G. Viscardi, A. Fin, *Adv. Funct. Mater.*, 2024, **35**, 2411230.

25 J. M. Fisher, M. L. Williams, J. R. Palmer, N. E. Powers-Riggs, R. M. Young, M. R. Wasielewski, *J. Am. Chem. Soc.*, 2024, **146**, 9911−9919.

26 (a) W. Zeng, Q. Qi, J. Wu, *Sci. Bull*., 2015, **60**, 1266–1271. (b) T. Shen, Y. Zou, X. Hou, H. Wei, L. Ren, L. Jiao, J. Wu, *Angew. Chem. Int. Ed.*, 2023, **62**, e202311928.

27 J. Feng, Y. Wu, Q. Yu, Y. Liu, W. Jiang, D. Wang, Z. Wang, *CCS Chem.*, 2020, **2**, 271–279.

28 (a) X. Chen, K. M. Engle, D.-H. Wang, J.-Q. Yu, *Angew. Chem. Int. Ed.*, 2009, **48**, 5094–5115. (b) R. Li, L. Jiang, W. Lu, *Organometallics* 2006, **25**, 5973-5975.

29 Y. Zhang, S.H. Pun, Q. Miao, *Chem. Rev.*, 2022, **122**, 14554–14593.

30 Y. Zou, Y. Han, S. Wu, X. Hou, C. H. E. Chow, J. Wu, *Angew. Chem. Int. Ed.*, 2021, **60**, 17654-17663.

31 Deposition Numbers 2491985 (for **3**), 2491986 (for **4**), 2491987 (for **7**), 2491988 (for **1a-*meso***), 2491989 (for **1b**), and 2491990 (for **1c**) contain the supplementary crystallographic data for this paper. These data are provided free of charge by the joint Cambridge Crystallographic Data Centre and Fachinformationszentrum Karlsruhe Access Structures service.

32 (a) D. Donaldson, J. M. Robertson, J. White, *Proc. R. Soc. London, Ser. A*, 1953, **220**, 311−321; (b) A. Camerman, J. Trotter, *Proc. R. Soc. London A*, 1964, **279**, 129−146.

33 J. Tanaka, *Bull. Chem. Soc. Jpn.*, 1963, **36**, 1237-1249.

34 J. V. Caspar, T. J. Meyer, *J. Phys. Chem.*, 1983, **87**, 952-957.

35 (a) Y. Nakakuki, T. Hirose, H. Sotome, M. Gao, D. Shimizu, R. Li, J.-Y. Hasegawa, H. Miyasaka, K. Matsuda, *Nat. Commun.*, 2022, **13**, 1475; (b) T. Shen, D. Dijkstra, A. Farrando-Pérez, P. G. Boj, J. M. Villalvilla, J. A. Quintana, Y. Zou, X. Hou, H. Wei, Z. Li, Z. Sun, M. A. Díaz-García, J. Wu, *Angew. Chem. Int. Ed*., 2023, **62**, 202304197.

36 (a) M. Ghasemlou, N. PN, K. Alexander, A. Zavabeti, P. C. Sherrell, E. P. Ivanova, B. Adhikari, M. Naebe, S. K. Bhargava, *Adv. Mater.*, 2024, **36**, 2312474; (b) Z. Yang, T. Xu, H. Li, M. She, J. Chen, Z. Wang, S. Zhang, J. Li, *Chem. Rev.*, 2023, **123**, 11047−11136.

37 (a) Y. Wu, J. Liu, G. Yang, Z. Bin, J. You, *J. Am. Chem. Soc.*, 2025, **147**, 19305−19314; (b) W. Jiang, H. Zhang, X. Hua, Y. Ma, Y. Feng, C. Yuan, Z. Liu, H.-L. Zhang, X. Shao, *Angew. Chem. Int. Ed.*, 2025, **64**, e202500391; (c) X. Tian, Z. Fan, Z. Li, S. Zhang, Z. Li, X. Zhuang, Y. Wang, C. Dou, *Angew. Chem. Int. Ed.*, 2025, **64**, e202500110; (d) Q. Wang, H. Zhang, J. Zhou, H. Dai, M. Mai, T. Huang, L. Wang, X. Wang, D. Zhang, L. Duan, *Adv. Mater.*, 2025, **37**, 2503839; (e) Q. Jin, M. Du, Y. Zhang, L. Duan, *Adv. Optical Mater.*, 2024, **13**, 2402918.

38 T. Mori, *Chem. Rev.*, 2021, **121**, 2373–2412.

39 (a) J. Li, C. Hou, C. Huang, S. Xu, X. Peng, Q. Qi, W.-Y. Lai, W. Huang, *Research (Wash D C)*, 2020, **22**, 3839160; (b) Q. Xu, M. Wang, Y. Liu, *Molecules*, 2025, **30**, 44; (c) Z. Zhou, M. A. Petrukhina, *Chem. Sci.*, 2025, **16**, 468−479; (d) C. A. Guido, F. Zinna, G. Pescitelli, *J. Mater. Chem. C*, 2023,**11**, 10474-10482; (e) H. Kubo, T. Hirose, T. Nakashima, T. Kawai, J. Hasegawa, K. Matsuda, *J. Phys. Chem. Lett.*, 2021, **12**, 686–695.

40 (a) Q. Zhou, X. Hou, J. Wang, Y. Ni, W. Fan, Z. Li, X. Wei, K. Li, W. Yuan, Z. Xu, M. Zhu, Y. Zhao, Z. Sun, J. Wu, *Angew. Chem. Int. Ed.*, 2023, **62**, e202302266; (b) Q. Zhou, W. Yuan, Y. Li, Y. Han, L. Bao, W. Fan, L. Jiao, Y. Zhao, Y. Ni, Y. Zou, H.-B. Yang, J. Wu, *Angew. Chem. Int. Ed.*, 2024, **63**, e202417749.

View Article Online
DOI: 10.1039/D6SC00676K

- All data supporting this study are provided in the Electronic Supporting Information (ESI)
- The X-ray crystallographic data were deposited in the Cambridge Crystallographic Data Centre (CCDC) with deposition numbers 2491985 (for **3**), 2491986 (for **4**), 2491987 (for **7**), 2491988 (for **1a-meso**), 2491989 (for **1b**), and 2491990 (for **1c**).
- Data available on request from the authors.